Array Optimisation for Wave Damping and Wave Absorption

Clotilde Nové-Josserand[#1], Ramiro Godoy-Diana[#2], and Benjamin Thiria[#3]

[#]*Laboratoire de Physique et Mécanique des Milieux Hétérogènes (PMMH)*
CNRS UMR 7636, ESPCI Paris, PSL Research University, Sorbonne Universités
7 Quai Saint Bernard, 75005 Paris, France
E-mail: clotilde.nove-josserand@espci.fr

Abstract—**Considerable work has been undertaken for the improvement of Wave Energy Converters (WEC) and array design. The present work focuses on the local effects of wave-structure interactions within an array of oscillating absorbers in order to optimise energy absorption. We use a model system of flexible blades, subject to monochromatic waves and develop a simplified one-dimensional model in order to predict optimal configurations, depending on various parameters, which include the number of blades and spacing. Optimal configurations are found to converge towards both regular and irregular arrays, depending on array size and on the choice of local parameters. These optimal arrays are found to increase global forcing by up to 5% compared to regular arrays.**

Keywords—**Wave energy converter, array optimisation, wave-structure interaction, flexibility, wave damping.**

I. Introduction

Ocean waves present a large potential for renewable energy that could reach 2TW [1]. Yet, only a small portion is thus far harvested and mostly through early-stage prototypes [2]. Additionally, when this energy is not harvested, it is transmitted to the shoreline where it can cause coastal erosion. Absorbing the energy of waves through converters therefore presents a double advantage.

A large effort has been made in the last two decades regarding the development of wave energy converters (WEC), with many proposed designs (see [3], [4], [5] for reviews). These devices remain nonetheless limited in power output and efficiency and, thus, deployments in large arrays will be necessary. Each device can then be impacted by the presence of neighbours, due to wave interferences.
Many studies have explored the influence of array configurations on WEC performance and have highlighted the possible strong interferences between waves within the array [6]–[11]. In fact, one interesting phenomenon is observed when the devices are placed in regular patterns, separated by a distance equal to half the wavelength of the incoming wave. In this case, strong reflection is observed, similar to the Bragg resonance seen in wave scattering through crystal lattices [12]. This strong effect has been the source of extensive research in areas of solid-state physics and acoustics, with specific interest for the development of metamaterials that could absorb waves efficiently [13]. This research can also be extended to water waves [14] and could apply to WEC farm design. Indeed, these arrays could also serve to dampen waves and reduce coastal erosion since their aim is to extract the energy of waves over large surface areas [15]–[17]. In this sense, Bragg resonance could be very useful. Yet, while the associated array configuration could benefit wave damping, it is also found to reduce the device oscillations, thereby limiting power extraction. This was observed experimentally by [18] and numerically by [19]. The latter developed an analytical model describing the interaction of waves and an array of small wave energy converting buoys. Band gaps and array power absorption were predicted using the Froude-Krylov approximation to model the force on a WEC element and multiple scale analysis. The results demonstrated a clear reduction of the array's efficiency in case of Bragg resonance. Similarly, [20] studied the effect of lateral spacing of flap-type converters on the resulting capture factors. Results showed very clear peaks in performances. These observations highlight the difficulty in designing optimal wave farms, which will have to result from a trade-off between wave damping and energy harvesting.

The study of array optimisation has been undertaken by a number of numerical studies, based on various applied mathematical tools. A recent semi-analytical model has for example been developed by [21] in order to test configurations that minimise power fluctuations. However, most optimisation studies thus far have been limited to small arrays or to specific conditions, due to the costly and heavy numerical calculations used. It is therefore difficult to obtain general conclusions. In this paper, we develop a simple one-dimensional interference model in order to evaluate the benefit of optimal array configurations in terms of wave energy absorption. Following an experimental validation using a small-scale array of flexible blades, both regular and irregular arrays are considered and the influence of local coefficients on global performances are discussed.

II. Methods

A. Theoretical model

Based on the small-scale experiments presented in [18], this paper studies the interaction between planar monochromatic waves and an infinite array of partially-submerged slender flexible blades. The total energy dissipated through the mechanical bending of these elastic structures is evaluated, depending on row spacings l_n. (see Fig. 1).
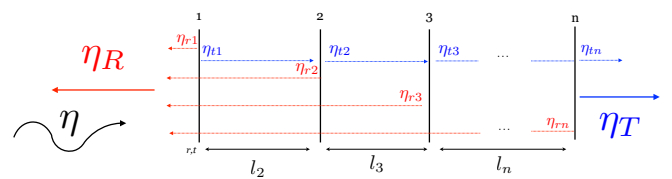

Fig. 1. Sketch of 1D model

1) Scaling: Each flexible blade within the array is subject to both inertial and viscous forces due to its interaction with water waves. This is expressed as:

$$\sum \underline{F}_{ext} = \underline{F}_{viscous} + \underline{F}_{inertia} = \underline{F}_{viscous} + \iint_S p\underline{n}dS \quad (1)$$

where p is the pressure due to the fluid acting on the wetted surface S in the normal $\underline{n}$ direction. Assuming potential flow, the pressure term is further expressed as:

$$p = \iint_S -\rho\left(\frac{\partial \Phi}{\partial t} + gz\right)\underline{n}\,dS \tag{2}$$

$$\Phi = \Phi_I + \Phi_D + \Phi_R \tag{3}$$

where Φ is the total wave potential such that fluid velocities can be written $\underline{u} = \nabla\Phi$, which includes an incident term Φ_I, a diffracted term Φ_D and a radiated term Φ_R. Total inertial forces are therefore shared between hydrodynamic forces in the undisturbed waves (Froude-Krylov force) and hydrodynamic forces due to the structure disturbing the waves (diffraction and radiation forces). The importance of each force term can be evaluated using two dimensionless numbers: the Keulegan-Carpenter number $KC = \frac{uT}{D}$, which compares viscous terms to inertial terms, and the diffraction number $\mathcal{D} = \frac{D}{\lambda}$, which divides the size of the object by the wave length. Note that $u = |\underline{u}|$ is the orbital velocity of the fluid particles, T is the wave period, D is the characteristic size of the object, and λ is the wave length.

Flap-type wave energy converters can be described as line absorbers and rely on inertially driven forces. Therefore, they are generally associated with low KC numbers and tend to be wide objects in order to maximise their capture width and efficiency. Diffraction thus plays an important role in the array forces.

2) Interference model: Let η be the incident complex waveform with amplitude a, wave number k and angular frequency ω. As this wave travels through the array, it will interact with each row n of blades, which behave as obstacles transmitting part of the wave with a local coefficient t and reflecting another part with a local coefficient r (c.f. figure 1).

Considering a 1D-case, each row is then subject to the sum of forces induced by waves traveling in the two opposing directions. We take incident and transmitted (η_t) waves traveling in the positive x-direction and reflected waves (η_r) traveling in the negative x-direction. The associated horizontal wave particle motions are illustrated in figure 2 (a) and (b) below:

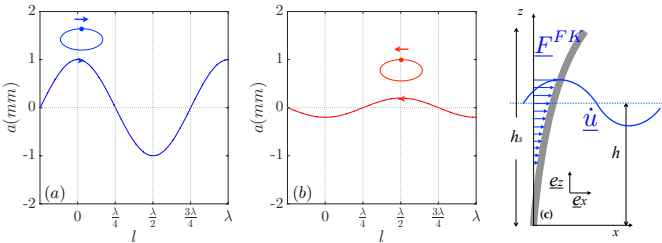
Fig. 2. Illustration of incident (or transmitted) (a) and reflected (b) waves with associated horizontal wave particle motion x. Sketch of the distributed Froude-Krylov wave force $\underline{F}^{FK}$ associated with the incident (or transmitted) wave on a partially submerged flexible blade (c).

Two waves traveling in opposite directions force water particles to move in opposite circular trajectories. Taking the transmitted wave $\eta_t = \Re\{tae^{i(kx-\omega t)}\}$ and reflected wave $\eta_r = \Re\{rae^{i(kx+\omega t)}\}$, the corresponding dynamic Froude-Krylov forces can be written as:

$$\underline{F}_t^{FK} = M\underline{\dot{u}}_t = F_t^{FK} \cdot \underline{e}_x \tag{4}$$

$$\underline{F}_r^{FK} = M\underline{\dot{u}}_r = F_r^{FK} \cdot (-\underline{e}_x) \tag{5}$$

where M is the mass of the displaced fluid, $\underline{\dot{u}}_t$ and $\underline{\dot{u}}_r$ are the orbital accelerations of the water particles associated to the transmitted and reflected waves, and $\underline{e}_x$ is taken to be the unit vector in the positive

x-direction (c.f. figure 2 (c)). For constant water depth, wave length and wave number, $\dot{u} = |\underline{\dot{u}}| \propto a$ and the total force $\underline{F}_{tot}^{FK}$ acting on the front row becomes:

$$\underline{F}_{tot}^{FK} = \sum \underline{F}^{FK} = \underline{F}_t^{FK} + \underline{F}_r^{FK} = \mathcal{A}^{FK} \cdot \underline{F}_i^{FK} \tag{6}$$

where $\mathcal{A}^{FK}$ is an amplification factor of the incident dynamic Froude-Krylov force $\underline{F}_i^{FK}$, resulting from array interferences.

In the more general case, any row n of an array composed of N rows will be subject the total wave force F_n^{FK} resulting from interfering transmitted (or incident) and reflected waves from the array:

$$\underline{F}_n^{FK} = \mathcal{A}_n^{FK} \cdot \underline{F}_i^{FK} \tag{7}$$

$$\mathcal{A}_n^{FK} = |T_n - R_n| \tag{8}$$

where the resulting R_n and T_n coefficients are obtained, as follows, from the sums of geometric series:

$$R_n = \underbrace{\frac{rt^n e^{i[\sum_{m=1}^n \varphi_m + 2\varphi_{(n+1)}]}}{1 - r^2 e^{i2\varphi_{(n+1)}}}}_{\text{immediate neighbours}} \underbrace{\sum_{k=0}^{N-n} t^{2k} e^{i2\sum_{m=n+2}^{k+2} \varphi_m}}_{\text{subsequent rows}} \tag{9}$$

$$T_n = \frac{t^{(n-1)} e^{i\sum_{m=1}^n \varphi_m}}{1 - r^2 e^{i2\varphi_n}}$$

where $\varphi_n = \frac{l_n 2\pi}{\lambda}$ corresponds to the phase shift of incident transmitted waves η_{tn} at row n with respect to the incident wave η.

The global force amplification factor resulting from array wave interferences can therefore be predicted using equation 8 and provides an indication on the local excitation force applied onto each row.

3) Energy dissipation K_d: At the local scale of a single row, the energy associated to the incident wave is shared between a reflected part of ratio r, a transmitted part of ratio t, and a dissipated part of ratio $k_d = 1 - (r + t)$. The dissipated energy depends on the device oscillations and includes terms of internal dissipation due to the device's restoring force (elastic bending or Power Take-Off damping) and external dissipation due to the added damping caused by the presence of the fluid (added mass and friction).

The device is modeled as a cantilevered flexible beam (c.f. Fig. 3 (c)) bending on its first mode of deformation, for which the motion is described by that of a damped oscillator. Assuming small oscillations, linear beam theory applies, suggesting that the local position of the blade $x(z,t)$ is a function of the maximal blade tip deflection $\underline{X}(t)$ and is proportional to the total beam loading and the elastic restoring force:

$$x(z,t) = \underline{v}_1(z) \cdot \underline{X}(t) \tag{10}$$

$v_1(z)$ is the local deflected shape and is further expressed as follows:

$$\begin{aligned} v_1(z) = \frac{1}{2}\bigg[&\cos(k_1 z) - \cosh(k_1 z) \\ &+ \left(\frac{\sin(k_1 h_s) - \sinh(k_1 h_s)}{\cos(k_1 h_s) - \cosh(k_1 z)}\right)(\sin(k_1 z) - \sinh(k_1 z))\bigg] \end{aligned} \tag{11}$$

where h_s is the total length of the blade, k_1 is the first root of the beam deflection equation. The power associated with internal and external dissipation can then be written as :

$$\mathcal{P} = 2[\Gamma_{int}(m + m_a)\dot{x}^2 + \Gamma_{ext}(m + m_a)\dot{x}^2] \tag{12}$$

$$\tag{13}$$

where Γ_{int} and Γ_{ext} are damping coefficients related to the internal and external work of the oscillator, m and m_a are respectively the mass of the beam and the added mass of the fluid displaced by the submerged part of the beam, and $\dot{x}$ is the blade tip velocity. For any given beam geometry and mechanical properties, and any imposed

[Hz]	a[mm]	λ[cm]	h[cm]
5	0.7	7.16	8

h_s[cm]	D[cm]	e[μm]	E[GPa]	ρ[kg/m³]
9	1.4	350	5	1380

wave conditions, the dissipated power is therefore proportional to the oscillation amplitudes. The power of incoming waves per unit area is given by: $\mathcal{P}_w = \frac{1}{2}\rho g a^2 \cdot v_g$, where v_g is the group velocity of the wave, and is related to phase velocity through $v_g = \frac{v_p}{2}(1 + \frac{2kh}{\sinh 2kh})$. The ratio of dissipated energy is then given by:

$$K_d = \frac{P}{P_w} = \frac{\Gamma_{int}(m+m_a)\dot{x}^2 + \Gamma_{ext}(m+m_a)\dot{x}^2}{\frac{1}{2}\rho g a^2 \cdot v_g} \quad (14)$$

From equations 10 and 14, one can easily notice that $K_d \propto \dot{x}^2 \propto X^2$. Therefore, the global absorption factor will also depend on the amplification factor as follows:

$$k_d(X^2) = 1 - (r^2 + t^2) \quad (15)$$

$$K_d = \sum_{n=1}^{N} \mathcal{A}_n^2 k_d \quad (16)$$

Using the amplification factor model, maximal potential energy dissipation is predicted using equation 16 above, based on the array layout.

In order to highlight the effect of the array on the global energy dissipation coefficient K_d, the results are compared to a theoretical reference coefficient $K_{d_{ref}}$, which we define as the sum of non-amplified individual dissipation coefficients, only taking into account cumulative reduced transmission throughout the array. This is expressed as:

$$K_{d_{ref}} = \sum_{n=0}^{N-1} t^{2n} k_d = k_d \cdot \frac{1 - t^{2N}}{1 - t^2} \quad (17)$$

Note that the transmission coefficient is squared since the dissipation coefficient is a function of X^2 (c.f. equations 10 and 14).

B. Experimental validation

In order to validate the model, small-scale experiments were run using an array of flexible slender blades subjected to a surface water wave field created in a wave canal 0.6 m wide and 1.8 m long. A flapping type wave maker was used to create controlled monochromatic waves and an angled polymer (PVC) sheet was placed at the end of the canal to act as a beach and minimise wall reflections. A sketch of the experimental set-up is presented in figure 3 (a). The blades were made from Mylar® material of thickness 350 μm, density 1380 kg.m⁻³ and Young's Modulus (E) 5 GPa. Individual Mylar® blades were fixed to Lego® blocks, which were arranged on a Lego® base board, thus allowing for easy configuration variations. Experiments were run at the natural resonant frequency of the blades, measured to be $f_0 = 5Hz$ in water. The blades were 9 cm long (h_s), fixed to a lego block of 1cm height and a base of 5mm thickness. The water depth was chosen to match capillary-gravity conditions, and was kept at 8cm, thus giving a submergence ratio of $h/h_s = 0.83$ (c.f. figure 3 (c)). The lateral spacing d between neighbouring blades was fixed at $\lambda/2$ (equal to 4 lego spaces, of 8mm each). Wave and blade characteristics are summarised in tables I and II, respectively.

In these conditions, the Keulegan-Carpenter number KC is of $\mathcal{O}(10^{-1})$, and the diffraction number D/λ is around 0.2, suggesting that inertia forces are dominating and array diffraction is not negligible. Our model therefore applies.

Two sets of experiments were run:

- The number of rows N was set to 2 and longitudinal spacing l_2 between rows 1 and 2 was varied over the range $[\frac{\lambda}{4}; \lambda]$.
- The number of rows N was set to 3 and longitudinal spacing l_3 between rows 2 and 3 was varied over the range $[\frac{\lambda}{4}; \lambda]$. Spacing l_2 between rows 1 and 2 was fixed equal to $\frac{\lambda}{4}$.
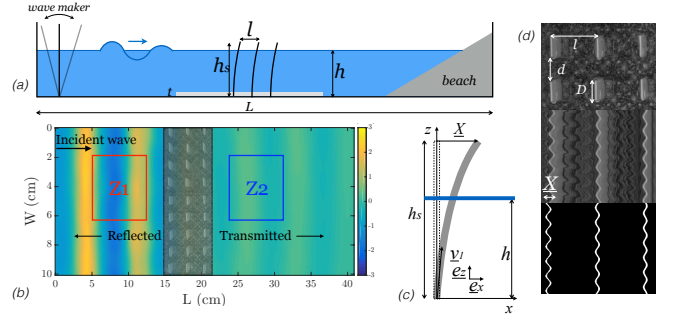

Fig. 3. (a) Sketch of the experimental set-up. (b) Example of a typical treated surface wave-map, before and after the blades, with selected zones of analysis $Z1$ (red) and $Z2$ (blue) for K_r and K_t measurements. (c) Sketch of the cantilever beam model. (d) Characteristic parameters of blades (top) and spatio-temporal plots (bottom) used for blade tip tracking analysis (please refer to [18] for detailed method description).

For each configuration, 400 images were recorded using a Phantom V9 camera at recording frequency of 200 fps, therefore covering 10 wave periods. In order to avoid strong lateral reflections and canal modes, recordings were launched when the first waves have traveled through the camera field. The surface wave maps were treated using the synthetic Schlieren method [22]. Transparent Lego base and blocks were used in order to benefit from this method over the entire image. Global reflection K_r and transmission K_t coefficients are then calculated from these treated surface wave maps, using two separate zones of analysis before ($Z1$) and after ($Z2$) the array (c.f. figure 3 (b)). It is assumed that the transverse average of the waves in each zone takes the form (equation 18):

$$\eta(x) = \begin{cases} ae^{-ikx} + K_r ae^{ikx} & \text{in } Z1 \\ K_t ae^{-ikx} & \text{in } Z2 \end{cases} \quad (18)$$

Taking x_a and $x_b \in Z1$, and $x_c \in Z2$, the reflection (K_r) and transmission (K_t) coefficients can then be defined as (equations 19 and 20):

$$K_r = \frac{e^{-ikx_b} - H_1 \cdot e^{ikx_a}}{H_1 \cdot e^{ikx_a} - e^{ikx_b}} \quad (19)$$

$$K_t = \frac{e^{-ikx_a} + K_r \cdot e^{ikx_a}}{H_2 \cdot e^{-ikx_c}} \quad (20)$$

where H_1 and H_2 are transfer functions defined as $\eta(x_b)/\eta(x_a)$ and $\eta(x_a)/\eta(x_c)$, respectively. All three points x_a, x_b, x_c were selected randomly and final coefficients were averaged over 200 iterations.

Finally, the calculated transmission coefficient K_t of each configuration is normalised by that calculated for a reference case without blades K_{t0} (giving $\tilde{K}_t$), in order to separate array damping from natural wave dissipation. A reference case (without blades but with the base board) was therefore taken at the end of each set of

experiments. These coefficients were calculated over the central area of the tank, where imposed waves are linear and monochromatic, thus justifying transverse averaging. The results obtained for a single row are: $K_r \approx 0.2$ and $\tilde{K}_t \approx 0.7$. These coefficients are those used for local r and t value inputs in the model.

The second part of the analysis was focused on the bending of the blades, which relies on the recording of the beam movements. The top of each blade was highlighted with white tape in order to contrast with the dark dotted pattern used for the Schlieren method. The movement of each blade end was quantified using a spatio-temporal stacking method as provided by the software package ImageJ, (see figure 3 (d)). We can therefore compare normalised blade oscillations $\tilde{X}$ for each row, with normalised wave forcing $\tilde{F}^{FK}$ for each row. This is represented by the amplification factor $\mathcal{A}$ for both quantities. Results for both sets of experiments are presented in figures 4 (a) and (b) below. It should be noted that the experimental results are plotted against l/λ, where λ is found to vary between $[0.065 - 0.07]$. This may lead to a slight shift of the curves.
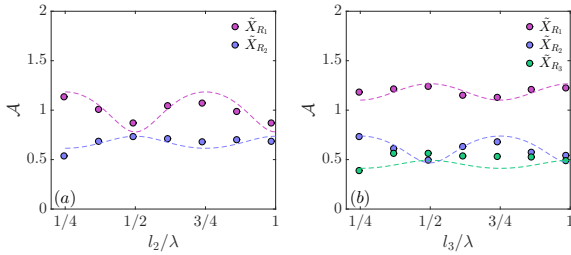

Fig. 4. Normalised blade oscillations $\tilde{X}$ (dots) for each row R_n of an array composed of 2 (b) and 3 rows (d) rows compared with numerical values of $\mathcal{A}_n$ calculated from equation 8 (dotted lines). Spacings l_2 in the case of $N = 2$ and l_3 in the case of $N = 3$ are varied within $[\frac{\lambda}{4}; \lambda]$.

Results show good agreement between experimental data and model predictions regarding blade oscillation amplification factors $\mathcal{A}$, with clear peaks and troughs at $l = \lambda/4$ and $l = \lambda/2$, as expected. The forcing applied on each row due to array interferences is well represented by the model and can be used to predict oscillation variations within various arrays.

III. RESULTS & DISCUSSION

We now use the model described above to explore all possible array configurations, in order to evaluate their influence on blade oscillations. The experiments presented in [18] showed a strong link between blade oscillations and wave damping. Indeed, when the spacing l was varied for an array composed of 4 rows, it was found that minimal global oscillations of blades at $l = \lambda/2$ led to a maximum in wave transmission and vice versa, when global oscillations at $l = \lambda/4$ were maximum, global transmission was minimum. This suggests that increasing blade oscillations is beneficial in terms of both energy absorption and energy damping. The model we have developed above can therefore be used in order to predict maximal global forcing of blades.

a) Regular configurations: We first compare two bounding cases for regular configuration patterns (i.e. arrays with constant spacing l between rows), which correspond to spacing ratios $l = \lambda/2$ and $l = \lambda/4$. Taking the same local coefficients as those measured experimentally ($r = 0.2$, $t = 0.7$), amplification factors calculated from equation 8 are plotted in figure 5 for each row as a function of the total number of rows in the array. The results are compared to a reference case without amplifications, i.e. assuming a series of single independent rows. These are represented by black asterisks and are calculated as t^{n-1} for each row n.

As expected, these results show the strong influence of the arrangement on front row oscillations, with a 30% decrease in values
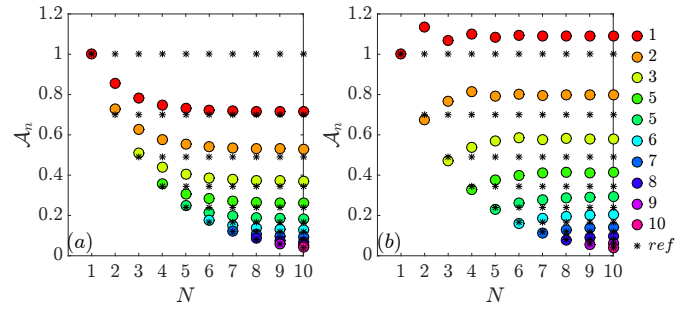

Fig. 5. Predicted amplification factors $\mathcal{A}_n$ for each row n of the array as a function or array size (increasing number of rows N). Results for constant array spacing $l = \lambda/2$ (a) and constant array spacing $l = \lambda/4$ (b). Theoretical oscillation factors without amplifications (reference) are presented in black asterisks.

for $l = \lambda/2$ versus a 10% increase for $l = \lambda/4$ and these effects hold true throughout the array, with similar attenuated effects for each subsequent row.

Another noticeable difference concerns the change in variations for increasing array sizes. While $\mathcal{A}_n$ decreases steadily with N for $l = \lambda/2$ before reaching a limit at N=5, it increases very slightly and in oscillatory form for $l = \lambda/4$. This oscillation is thought to come from a pairing effect of amplifications, with mimima observed for even arrays, and maxima for odd arrays.

b) Optimal configuration: It is clear that convergence rates and variations of amplification factors depend on the input parameters r and t, which are so far measured from experimental data. If these coefficients now become changeable, for example via a modification of the confinement ratio, or blade flexibility and shape, then these tendencies will be altered. Additionally, given that $\lambda/2 = 2 \times \lambda/4$ the benefits of $l = \lambda/4$ are diminished by the negative impact of $l = \lambda/2$ spacings on blade oscillations for arrays $N > 2$. This suggests that for larger arrays, configurations causing maximal oscillation amplifications is no longer regular, whereby the spacing between rows is no longer constant. These optimal configurations are determined by scanning all possible combinations of l_n spacings and calculating their associated amplification factors $\mathcal{A}_n$. The optimal array is that providing the maximal global amplification factor $\mathcal{A}_{tot} = \Sigma \mathcal{A}_n$.
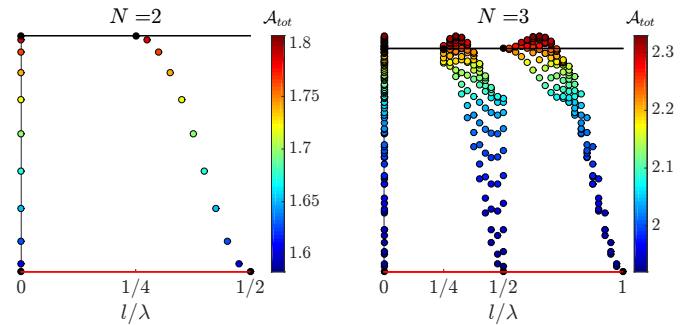

Fig. 6. Representation of all scanned array configurations as a function of the global amplification factor $\mathcal{A}_{tot}$ for arrays composed of N=2 (left) and N=3 (right) rows. Local parameters are taken as those measured experimentally, i.e., r=0.2 and t=0.7. As reference, regular arrays $l=\lambda/2$ and $l=\lambda/4$ are identified with red and black horizontal lines, respectively.

Figure 6 first presents all scanned configurations for array sizes of 2 and 3 rows, ordered as a function of their calculated cumulative amplification factors $\mathcal{A}_{tot}$. The optimal configurations are therefore

those at the top of the graphs and are compared to the two regular arrays $l = \lambda/4$ and $l = \lambda/2$ identified by means of black and red lines, respectively. Note that these results correspond to the fixed local parameters associated with the experimental data. As observed in the experimental results shown in figure 4 (a), the optimal configuration for a 2-row array converges to the regular case $l = \lambda/4$, with an overall increase of about 12.5% compared to the configuration $l = \lambda/2$. For an array composed of 3 rows, however, the optimal case converges towards an array that is slightly offset from the regular case $l = \lambda/4$, with $l_2 = 0.3\lambda$ and $l_3 = 0.35\lambda$. This illustrates the compromise between the benefit of spacing $l = \lambda/4$ over the front row of two successive rows and the advantage of $l = \lambda/2$ for the back row. The resulting optimum provides an increase of around 5% compared to the regular case $l = \lambda/4$.

Following the same procedure local parameters are now varied in order to explore the impact of optimal configurations on array performances. Fig. 7 presents the percentage increase in global dissipation coefficient K_d for optimal configurations compared to regular arrays $l = \lambda/2$ (left) and $l = \lambda/4$ (right), as well as the theoretical reference case (middle) (c.f. equation 17). The results are presented for increasing number of rows from $N=2$ to $N=8$ (top graphs) and for increasing reflection coefficient r (bottom graphs). Local dissipation values are in each case varied between 0.1 and 0.4.

Optimal configurations are seen to dissipate much more than regular arrays of $l = \lambda/2$ with an increase in K_d reaching up to 130% for an array of 8 rows (a). A large improvement is also noticeable compared to the reference case ($\approx$ 30% (b)). In both cases, values increase steadily with array size. When compared to regular array $l = \lambda/4$, optimal configurations are shown to improve global dissipation for uneven arrays only, and corresponding percentages decrease rapidly with values $\leq 1\%$ beyond $N=6$. These observations suggest that optimal configurations generally tend towards the regular array of $l = \lambda/4$ with negligible improvements limited to a maximum of nearly 6% reached for the specific case of $N=3$.

Variations of K_d for increasing r show global parabolic tendencies for which the inflexion point is shifted towards lower values as k_d increases. These points correspond to the cases where $r \approx t$, i.e. when local reflection and transmission has the same impact.

All maximum values are associated with local k_d coefficients equal to 0.1, i.e. in the case of maximal energy transmission towards neighbouring rows.
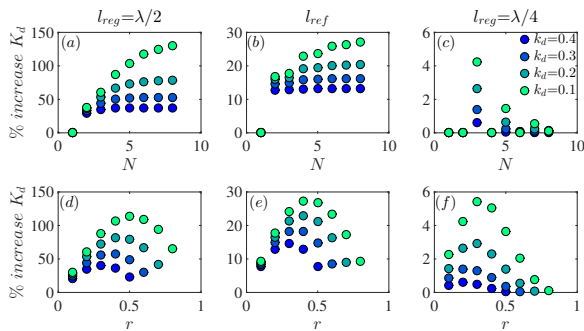

Fig. 7. Increased performance of optimal arrays compared to regular and reference configurations as a function of number of rows N for fixed $r = 0.2$ (a)-(c) and for increasing local coefficient r with fixed number of rows $N = 3$ (d)-(f). The local dissipation value k_d is varied between 0.1 and 0.4. Calculations are performed using equations 16 and 17.

IV. CONCLUSION

Following previous observations made regarding the influence of array configurations on wave absorber oscillations, this study has presented a simple one-dimensional model able to predict the effects of wave interferences on array performance. Based on known local reflection and transmission coefficients of an isolated row, this model was used to explore optimal array configurations regarding wave energy dissipation. Results have confirmed the previous experimental data by showing that in regular arrays, a separating distance $l = \lambda/2$ reduces blade oscillations, while the contrary is found for a separating distance $l = \lambda/4$. Predicted optimal configurations were found to vary between regular and irregular arrays, depending on the number of rows and on the values of the input parameters $\{r, t, k_d\}$. Increased amplification factors were found to reach up to 5.5% for cases composed of 3 rows, compared to the best regular cases and improve the least productive array by over 100%. Based on previous experimental results, this increase would not only improve wave energy extraction but also wave damping, thereby benefiting both purposes of the array. It should be noted that this simple interference model has been limited to monochromatic and unidirectional waves but could easily be adapted to more realistic conditions by using of the superposition principle and simple geometry. It could therefore serve array design for specific sites with associated wave spectra.

Further work is under way regarding the prediction of global reflection and transmission in order to predict the global energy distribution of such arrays. Additional experimental work is also required to further validate the model.

REFERENCES

[1] B. Drew, A. R. Plummer, and M. N. Sahinkaya, "A review of wave energy converter technology," 2009.

[2] A. Clément, P. McCullen, A. Falcão, A. Fiorentino, F. Gardner, K. Hammarlund, G. Lemonis, T. Lewis, K. Nielsen, S. Petroncini *et al.*, "Wave energy in europe: current status and perspectives," *Renewable and sustainable energy reviews*, vol. 6, no. 5, pp. 405–431, 2002.

[3] J. Falnes, *Ocean waves and oscillating systems: linear interactions including wave-energy extraction.* Cambridge university press, 2002.

[4] S. De Chowdhury, J.-R. Nader, A. M. Sanchez, A. Fleming, B. Winship, S. Illesinghe, A. Toffoli, A. Babanin, I. Penesis, and R. Manasseh, "A review of hydrodynamic investigations into arrays of ocean wave energy converters," *arXiv preprint arXiv:1508.00866*, 2015.

[5] A. Day, A. Babarit, A. Fontaine, Y.-P. He, M. Kraskowski, M. Murai, I. Penesis, F. Salvatore, and H.-K. Shin, "Hydrodynamic modelling of marine renewable energy devices: A state of the art review," *Ocean Engineering*, vol. 108, pp. 46–69, 2015.

[6] F. Dias, E. Renzi, S. Gallagher, D. Sarkar, Y. Wei, T. Abadie, C. Cummins, and A. Rafiee, "Analytical and computational modelling for wave energy systems: the example of oscillating wave surge converters," *Acta Mechanica Sinica*, pp. 1–16, 2017.

[7] A. Babarit, "On the park effect in arrays of oscillating wave energy converters," *Renewable Energy*, vol. 58, pp. 68–78, 2013.

[8] B. Borgarino, A. Babarit, and P. Ferrant, "Impact of wave interactions effects on energy absorption in large arrays of wave energy converters," *Ocean Engineering*, vol. 41, pp. 79–88, 2012.

[9] D. Sarkar, E. Renzi, and F. Dias, "Wave farm modelling of oscillating wave surge converters," in *Proc. R. Soc. A*, vol. 470. The Royal Society, 2014, p. 20140118.

[10] D. Sarkar, K. Doherty, and F. Dias, "The modular concept of the oscillating wave surge converter," *Renewable Energy*, vol. 85, pp. 484–497, 2016.

[11] Y. Wei, T. Abadie, A. Henry, and F. Dias, "Wave interaction with an oscillating wave surge converter. part ii: Slamming," *Ocean Engineering*, vol. 113, pp. 319–334, 2016.

[12] G. Arnaud, V. Rey, J. Touboul, D. Sous, B. Molin, and F. Gouaud, "Wave propagation through dense vertical cylinder arrays: Interference process and specific surface effects on damping," *Applied Ocean Research*, vol. 65, pp. 229–237, 2017.

[13] N. Kaina, M. Fink, and G. Lerosey, "Composite media mixing bragg and local resonances for highly attenuating and broad bandgaps," *Scientific reports*, vol. 3, p. 3240, 2013.

[14] X. Hu and C. Chan, "Refraction of water waves by periodic cylinder arrays," *Physical review letters*, vol. 95, no. 15, p. 154501, 2005.

[15] J. Abanades, D. Greaves, and G. Iglesias, "Coastal defence using wave farms: The role of farm-to-coast distance," *Renewable Energy*, vol. 75, pp. 572–582, 2015.

[16] E. Guazzelli, V. Rey, and M. Belzons, "Higher-order bragg reflection of gravity surface waves by periodic beds," *Journal of Fluid Mechanics*, vol. 245, pp. 301–317, 1992.

[17] L.-A. Couston, M. A. Jalali, and M.-R. Alam, "Sheltering the shore via nearshore oblique seabed bars," in *ASME 2016 35th International Conference on Ocean, Offshore and Arctic Engineering*. American Society of Mechanical Engineers, 2016, pp. V007T06A041–V007T06A041.

[18] C. Nové-Josserand, F. C. Hebrero, L.-M. Petit, W. Megill, R. Godoy-Diana, and B. Thiria, "Surface wave energy absorption by a partially submerged bio-inspired canopy," *Bioinspiration & Biomimetics*, 2018.

[19] X. Garnaud and C. C. Mei, "Bragg scattering and wave-power extraction by an array of small buoys," in *Proceedings of the Royal Society of London A: Mathematical, Physical and Engineering Sciences*. The Royal Society, 2009, p. rspa20090458.

[20] E. Renzi and F. Dias, "Relations for a periodic array of flap-type wave energy converters," *Applied Ocean Research*, vol. 39, pp. 31–39, 2013.

[21] M. Göteman, J. Engström, M. Eriksson, and J. Isberg, "Optimizing wave energy parks with over 1000 interacting point-absorbers using an approximate analytical method," *International Journal of Marine Energy*, vol. 10, pp. 113–126, 2015.

[22] F. Moisy, M. Rabaud, and K. Salsac, "A synthetic schlieren method for the measurement of the topography of a liquid interface," *Experiments in Fluids*, vol. 46, no. 6, p. 1021, 2009.